

# Anisotropic Growth of the Primary Dendrite Arms in a Single-Crystal Thin-Walled Nickel-Based Superalloy

Selina Körber, Michael Fleck, Rainer Völkl, and Uwe Glatzel\*

The influence of the withdrawal rate and wall thickness on the primary and secondary dendrite arm spacings of single-crystal specimens manufactured by the Bridgman process is investigated. Thin-walled specimens with wall thicknesses of 0.4, 0.8, 1, and 2 mm are compared with conventional cast single-crystal cylindrical specimens with a diameter of 15 mm of the nickel-based superalloy MAR M247LC. It is found that the average primary dendrite arm spacing decreases slightly with decreasing wall thickness, whereas the secondary dendrite arm spacing is relatively independent of the cast wall thickness. The slight decrease in primary dendrite arm spacing relates to an  $\approx 0.2$  mm wide boundary zone next to the ceramic mold/cast metal interface that is not only present in the thin-walled specimens, but also within cylindrical single-crystal specimens. Within this boundary zone, the primary dendrite arm spacing is anisotropic. While the spacing of two dendritic cores sitting aside each other ( $y$ -direction) remains at the bulk value, the spacing of two dendritic cores sitting in line with the interface normal ( $x$ -direction) is significantly reduced.

and secondary dendrite arm spacings. The spacings are linked to the mechanical behavior of the final parts and relate solidification conditions, such as the local temperature gradient and the solidification rate. Significant amount of research work in the literature is dedicated to the relation of these spacings to the process variables of directional solidification. For a recent review on the subject, the reader is referred to Strickland et al.<sup>[3]</sup>

Franke et al.<sup>[4,5]</sup> and Grudzień-Rakoczy et al.<sup>[6]</sup> studied the influence of thermo-physical properties, such as enthalpy of fusion, heat conductivity, and specific heat, on the solidification of nickel-based superalloys. The temperature gradient at the solidification front and the solidification rate plays a major role in the formation of as-cast microstructures. Casting nickel-based superalloys in a Bridgman furnace,

Liu et al.<sup>[7]</sup> showed that low withdrawal rates lead to a cellular-dendritic microstructure with blocky or rosette-like  $\gamma/\gamma'$ -eutectics, whereas high withdrawal rates lead to fine dendritic structures with fine  $\gamma'$ -precipitates. Milenkovic et al.<sup>[8]</sup> and Lee et al.<sup>[9]</sup> investigated the influence of different solidification conditions on the microstructure of directional solidified cylindrical specimens of the nickel-based superalloy M247LC and showed that an increase in the temperature gradient and solidification rate leads to decreasing dendrite arm spacings and accordingly to finer microstructures.

Zhang et al.<sup>[10]</sup> investigated the influence of the wall thickness on the dendritic structure of directionally solidified turbine vanes. They observed decreasing primary dendrite arm spacings in increasingly thinner casting geometries. Similar observations were made by Krawczyk and Bogdanowicz<sup>[11]</sup> in single-crystal cored turbine blades in the vicinity of the cooling bores. These areas with smaller primary dendrite arm spacings around the cooling bores are about 3–4 mm wide and already clearly indicate a dependence of the primary dendrite arm spacing on the wall thickness. These scales are still very large compared with the largest microstructure length scale in single-crystal casting of nickel-based superalloys, that is, the spacing of primary dendritic trunks, which is in our case between 0.3 and 0.4 mm. To the best of the authors' knowledge, there is no fundamental study available in the literature discussing microstructure effects in thin-walled single-crystal castings with wall thicknesses that reach the scale of the primary dendrite arm spacing.

In this work, the resulting primary and secondary dendrite arm spacings during thin-walled single-crystal solidification

## 1. Introduction

Over the last years, complex cooling channels inside hollow turbine blades as well as their trailing edges became increasingly thinner.<sup>[1]</sup> The wall thickness on the trailing edge of a turbine blade currently goes down to 0.2 mm.<sup>[2]</sup> In addition to weight savings, thinner structures are beneficial for aerodynamics and cooling. All these effects have beneficial impact on the efficiency of flight engines.

Quite often, these turbine blades are manufactured as single crystals by the Bridgman process. The final parts as well as the microstructure and mechanical properties result from the directional solidification of the metallic melt within the given casting geometry. The microstructure of directionally solidified single-crystal materials is usually characterized by the primary

S. Körber, M. Fleck, R. Völkl, U. Glatzel  
Metals and Alloys  
University of Bayreuth  
Prof.-Rüdiger-Bormann-Straße 1, 95447 Bayreuth, Germany  
E-mail: uwe.glatzel@uni-bayreuth.de

 The ORCID identification number(s) for the author(s) of this article can be found under <https://doi.org/10.1002/adem.202101332>.

© 2021 The Authors. Advanced Engineering Materials published by Wiley-VCH GmbH. This is an open access article under the terms of the Creative Commons Attribution License, which permits use, distribution and reproduction in any medium, provided the original work is properly cited.

DOI: 10.1002/adem.202101332

**Table 1.** Composition of MAR M247LC [wt%].

Ni	Cr	Co	Mo	W	Al	Ti	Ta	Hf	C	B	Zr
61.5	8.1	9.3	0.5	9.4	5.7	0.7	3.3	1.4	0.07	0.017	0.007

are systematically investigated, focusing on two important process parameters: the withdrawal rate and the cast wall thickness. Three different withdrawal rates are selected and the single-crystal dendritic solidification in very thin specimens with wall thicknesses down to 0.4 mm is studied. Furthermore, the thin-walled solidification behavior is compared with the single-crystal bulk solidification within a cylindrical specimen with 15 mm diameter.

## 2. Experimental Section

### 2.1. Single-Crystal Casting

The nickel-based superalloy MAR M247LC with the composition given in Table 1 was investigated. Batches of the masteralloy M247LC were positioned in a ceramic crucible and melted in an induction furnace under vacuum at a pressure of  $5 \times 10^{-2}$  Pa. A ceramic mold was positioned on a water-cooled copper chill plate and preheated to a temperature of 1450 °C. After pouring the molten material into the preheated mold, the ceramic mold was withdrawn through a water-cooled copper baffle, as described by Konrad et al.<sup>[12]</sup> The ceramic molds were produced by an adaptation of the standard lost-wax process using positive polymer models instead of wax.<sup>[13]</sup> The layers consisted of a slurry of colloidal silica bound by ZrSiO<sub>4</sub> and aluminum oxide particles with varying grain sizes. The innermost layer consisted of aluminum oxide particles with a grain size of 0.1 mm,

followed by four fine backup layers (0.25–0.5 mm) and four coarse backup layers (0.5–1 mm) of aluminum oxide particles.

In addition to conventional single-crystal cylindrical specimens with a diameter of 15 mm and a length of 120 mm, thin-walled single crystal specimens with wall thicknesses of 0.4, 0.8, 1, and 2 mm were cast. The single-crystal thin-walled specimens consisted of two different windows, each having the wall thicknesses of either 0.4 and 0.8 mm or 1 and 2 mm, see Figure 1a. Withdrawal rates were varied between 0.5, 3 and 6 mm min<sup>-1</sup> for each casting geometry, so a total of nine single crystal specimens were produced.

### 2.2. Specimen Preparation

Electron backscattered diffraction investigations on cross sections of the cast samples were carried out to determine the deviation of the crystal orientation with respect to the [1]-orientation. In any case the deviation of the single-crystal thin-walled specimens was less than 5°. The single-crystal cylindrical specimens were oriented using a goniometer. The cylindrical cross section of the cylindrical specimen was ground with SiC paper with grits of 500, 1000, and 2000 and etched with a solution of 3 g Mo-(VI)-oxide, 100 mL H<sub>2</sub>O, 100 mL HNO<sub>3</sub>, and 100 mL HCl to make the dendritic structure visible. Then, the cylindrical specimens were ground in the longitudinal direction and also etched, so the dendrites could be aligned vertically using a goniometer. The single-crystal cylindrical specimens were cut by electrical discharge machining longitudinally and perpendicular along the aligned dendrites to obtain longitudinal and cross sections of each oriented cylindrical specimen. This process is not possible for the thin-walled specimens as the possibilities for orientation were restricted by thin-walled volumes. In addition to a cross section, two longitudinal sections were prepared by

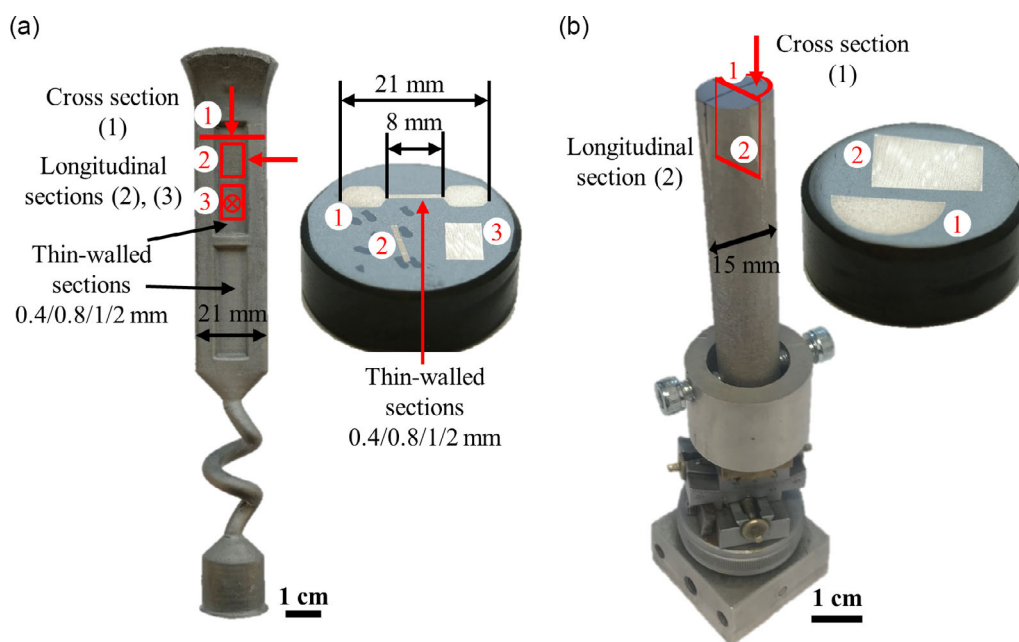


**Figure 1.** Geometry of cast samples and section positions of a) thin-walled specimen and b) single-crystal cylindrical specimen.

electrical discharge machining for the single-crystal thin-walled specimens for each wall thickness. The geometry of the two different casting samples and the section positions are exemplary shown in Figure 1.

The cut sections of the single-crystal cylindrical and also the thin-walled specimens were embedded in phenolic resin, ground by SiC paper with grits of 500, 1000, and 2000, polished with a diamond suspension, and finally etched again. For the examination of the dendrite arm spacings by means of optical microscopy, a Zeiss Axioplan in the reflecting light mode was used.

### 2.3. Methods for Evaluation

Primary dendrite arm spacings were determined using cross sections (surface normal parallel to growth direction) by measuring the distances between neighboring dendritic cores. Secondary dendrite arm spacings were determined using longitudinal sections (surface normal perpendicular to growth direction). This is schematically illustrated in Figure 2a.

Especially in the study of the anisotropy of the primary dendrite arm spacings due to the thin-walled geometry, distances between neighboring dendrite cores in  $x$ - and  $y$ -directions (perpendicular and parallel to the thin wall) were measured, see Figure 2b.

As a complement of these two evaluation methods, the area counting method<sup>[14]</sup> was applied for the determination of the primary dendrite arm spacing. Hence, cross-sectional macroimages

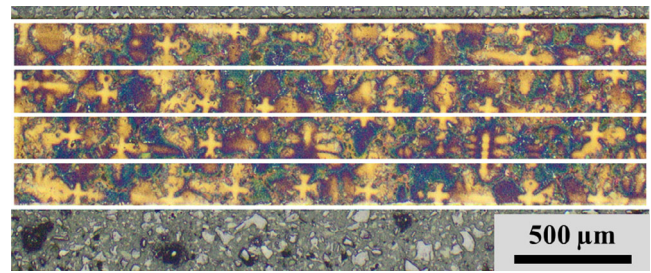


**Figure 3.** Cross section of a thin-walled specimen with a wall thickness of 0.8 mm, which is divided into four rectangles of equal size for the evaluation of the primary dendrite arm spacing by the area counting method.

were divided into rectangles of the equal area, which are exemplary shown in Figure 3 for a thin-walled specimen with a wall thickness of 0.8 mm.

The height of the rectangles was 0.2 mm, whereas the width was  $\approx 3$  mm. The height of 0.2 mm ensures that a sufficient number of dendrites can be counted in every rectangle and that cross sections of the thin-walled specimens in this study can be divided into even-numbered strips. The area counting method is described by Equation (1).

$$\lambda_p = (A/n)^{0.5} \quad (1)$$

where  $\lambda_p$  is the primary dendrite arm spacing and  $n$  is the number of dendrite cores in a defined area  $A$ .

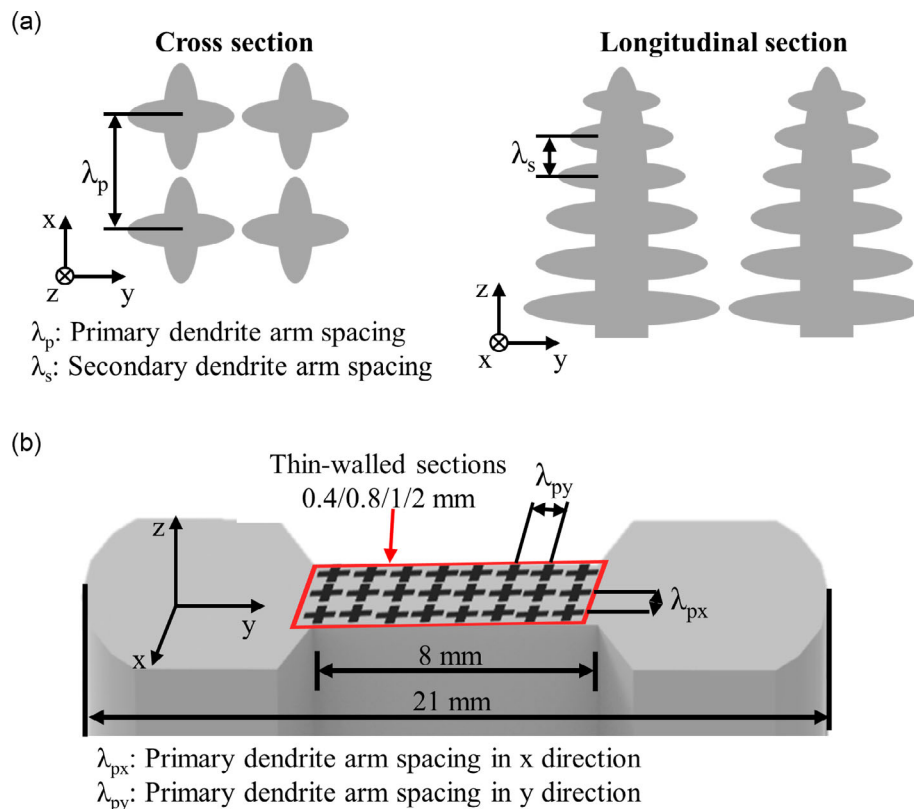


**Figure 2.** Schematic illustration of the determination of a) primary and secondary dendrite arm spacings of neighboring dendrites and b) primary dendrite arm spacings in the  $x$ - and  $y$ -direction between neighboring dendrite cores.

### 3. Results

Figure 4 shows the dendritic structures on cross and longitudinal sections of 0.4 mm thick thin-walled single-crystal specimens in comparison with single-crystal cylindrical specimens with 15 mm diameter. An increase in the withdrawal rate from 0.5 to 3 and 6 mm min<sup>-1</sup> (left to right) leads to significantly finer dendritic structures.

The dependence of the primary and secondary dendrite arm spacings on the withdrawal rate for all five specimen thicknesses is shown in Figure 5. As expected, a reduction of the withdrawal rate leads to higher primary and secondary dendrite arm spacings. The secondary dendrite arm spacing turns out to be independent from the cast wall thickness. The average primary dendrite arm spacing decreases slightly with decreasing wall thickness. This slight decrease results from a boundary zone of anisotropic reduced primary dendrite arm spacings, which becomes increasingly important with decreasing wall thickness.

This will become more clear in the following studies and is discussed in detail below.

The influence of the cast wall thickness on the primary dendrite arm spacing was further investigated at a withdrawal rate of 3 mm min<sup>-1</sup>. Primary dendrite arm spacings in *x*- and *y*-directions are plotted against the cast wall thickness in Figure 6a. It can be clearly seen that the primary dendrite arm spacings, especially with the extremely thin wall thicknesses of 0.4 and 0.8 mm, differ strongly in these two directions. With a wall thickness of 0.4 mm, the primary dendrite arm spacing  $\lambda_{py}$  in *y*-direction is by a factor of 1.6 higher than  $\lambda_{px}$  in *x*-direction. In contrast, the primary dendrite arm spacings  $\lambda_{px}$  and  $\lambda_{py}$  are equal for the single-crystal cylindrical specimen with a diameter of 15 mm. Figure 6b area 1 exemplary shows dendrites arranged very close to one another perpendicular to the wall, whereas the distance between the two adjacent dendritic cores in area 2 is significantly higher.

With the results described in Figure 6, it is clear that, in addition to the dependency between the primary dendrite arm

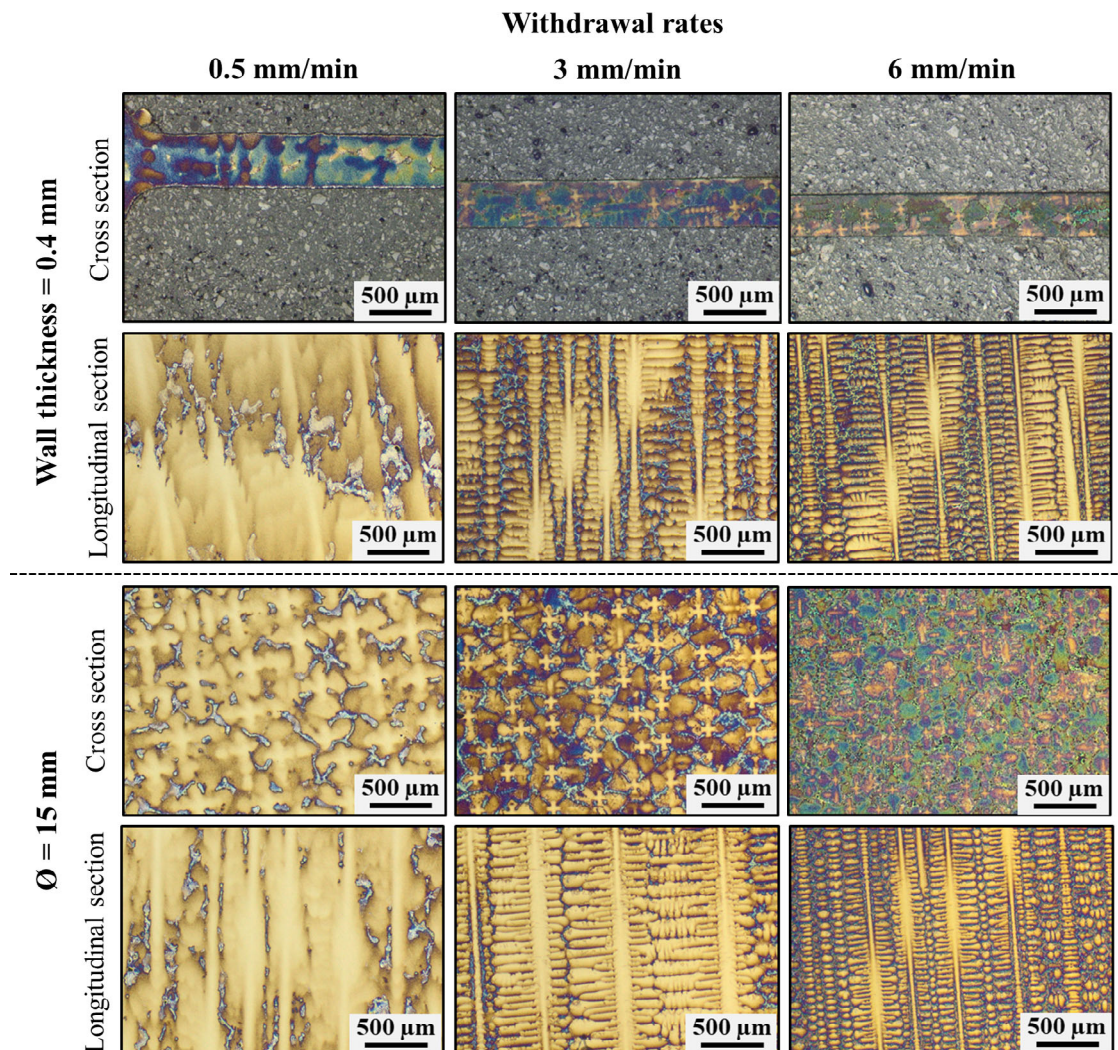


**Figure 4.** Light microscopic micrographs of dendritic structures on cross and longitudinal sections for thin-walled specimens with a wall thickness of 0.4 mm in comparison with a single-crystal 15 mm cylindrical specimen; from left to right increasing withdrawal rates during Bridgman single-crystal growing process.

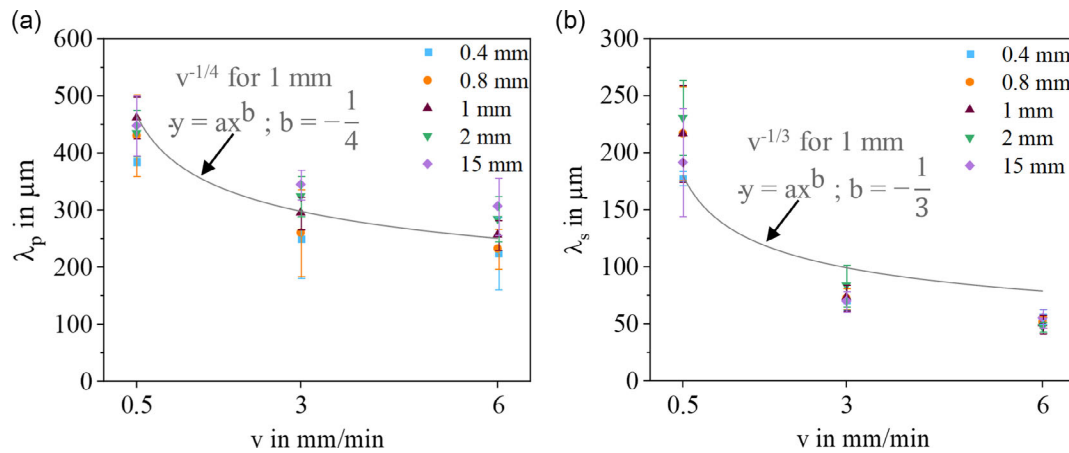


**Figure 5.** Influence of the withdrawal rate  $v$  and wall thickness on a) primary dendrite arm spacing  $\lambda_p$  and b) secondary dendrite arm spacing  $\lambda_s$ .

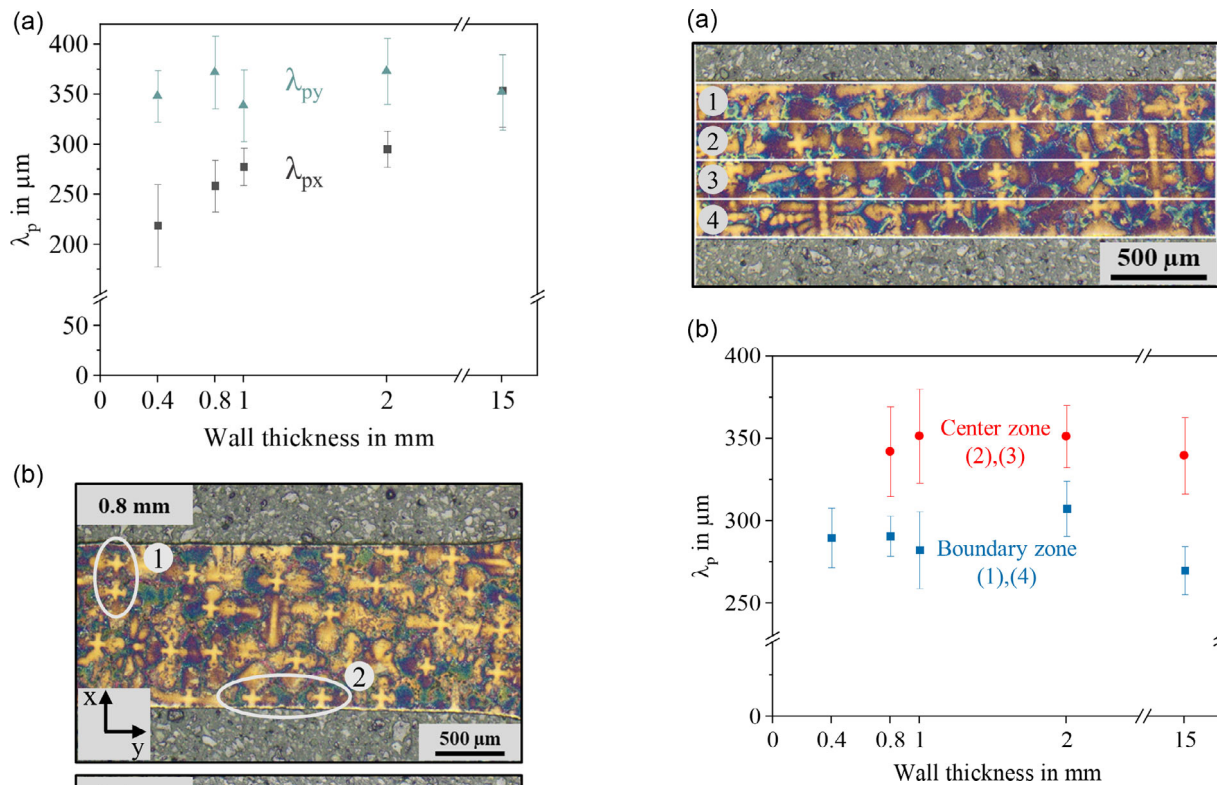


**Figure 6.** a) Primary dendrite arm spacing of pairs of neighboring dendritic cores in  $x$ - and  $y$ -direction at a withdrawal rate of  $3 \text{ mm min}^{-1}$ . b) Cross sections of thin-walled specimens with a wall thickness of 0.8 and 0.4 mm; to illustrate the determination method of primary dendrite spacings in  $x$ - (area 1) and  $y$ - (area 2) directions, two exemplary chosen pairs of dendritic cores are shown, as surrounded by gray circles.

spacing on the cast wall thickness, there is an anisotropy that leads to lower primary dendrite arm spacings in  $x$ -direction

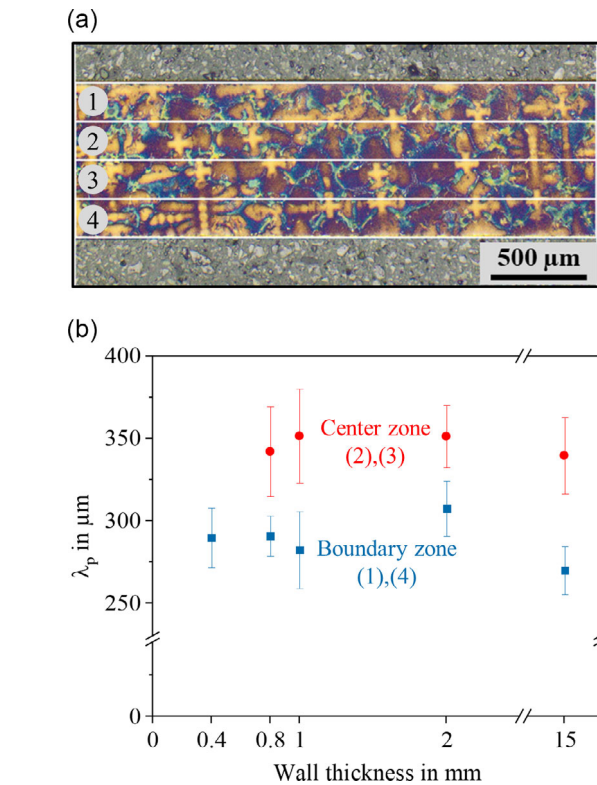


**Figure 7.** a) Cross section of a thin-walled sample with a wall thickness of 0.8 mm divided into four equal-sized rectangles, the boundary zone is exemplarily represented by rectangles 1 and 4 and the center area by rectangle 2 and 3. b) Primary dendrite arm spacings of the boundary and center area determined using the area counting method by dividing cross sections into rectangles of equal size.

(perpendicular to the thin wall). In order to investigate this anisotropy more closely, the macroimages of the cross sections are broken down into equal-sized rectangles (Figure 7a) and the primary dendrite arm spacings were determined using the area counting method for each rectangle, described with Equation (1). The height of the rectangles is 0.2 mm, which is slightly larger than half the undisturbed primary dendrite arm spacing. A

distinction is made accordingly between the boundary and center areas for all wall thicknesses except for 0.4 mm, as with this thin wall thickness no delimitation can be made between the boundary and center areas. Figure 7b shows that the primary dendrite arm spacings in the boundary areas are smaller compared with the center areas for all wall thicknesses.

#### 4. Discussion

In the theory of directional solidification, the temperature gradient at the solidification front and the solidification rate are generally regarded as the most important parameters. In the Bridgman process for single-crystal growth, the solidification rate is in good approximation constant over the solidification time and is identical to the withdrawal rate. Sahn et al.<sup>[15]</sup> derived the dependencies of the primary dendrite arm spacing,  $\lambda_p$ , and of the secondary dendrite arm spacing,  $\lambda_s$ , from the solidification rate,  $v$ .

$$\lambda_p \sim v^{-1/4} \quad (2)$$

$$\lambda_s \sim v^{-1/3} \quad (3)$$

The primary and secondary dendrite arm spacings observed in this investigation do both indeed increase with the withdrawal rate, see Figure 5. The fits shown in Figure 5 illustrate the dependency of the primary and secondary dendrite arm spacings on the withdrawal rate, which is also described by Equation (2) and (3). An increase in the withdrawal rate leads to a reduction in the primary and secondary dendrite arm spacings. The dependency of the primary dendrite arm spacing on the withdrawal rate is in good agreement with the fit described by Equation (2). In contrast to that there are differences in the fit described by Equation (3) for the secondary dendrite arm spacing, which is due to the higher standard deviation at a withdrawal rate of 0.5 mm min<sup>-1</sup>. The dependency of primary and secondary dendrite spacings from the withdrawal rate is in good agreement with the results of Elliott et al.<sup>[16]</sup> and Zhou et al.<sup>[17]</sup>. They investigated the influences of the process parameters during directional solidification on the dendrite arm spacing of the nickel-based superalloys IN792 and RENÉ N4. The primary and secondary dendrite arm spacings of the cylindrical specimen with 15 mm diameter measured in this work at a withdrawal rate of 3 mm min<sup>-1</sup> are in good accordance with the results of Whitesell et al.<sup>[18,19]</sup>. They measured a primary dendrite arm spacing of 350  $\mu\text{m}$  and secondary dendrite arm spacing of about 80  $\mu\text{m}$ .

The influence of the wall thickness on the solidification microstructure during single-crystal casting within the Bridgman process was discussed earlier. Grudzień-Rakoczy et al.<sup>[6]</sup> and Franke et al.<sup>[5]</sup> mentioned that the temperature gradient on the surface of thin-walled specimens is higher and decreases with growing distance to the surface. Goldschmidt<sup>[20]</sup> investigated the working range regarding temperature gradient and withdrawal rate for the single-crystal solidification of the nickel-based superalloy SRR 99 and showed that the temperature gradient at the solidification front decreases with an increase in the ingot cross section. This correlates with the decreasing primary dendrite arm spacing at decreasing wall

thicknesses in this work. Zhang et al.<sup>[10]</sup> reported decreasing primary dendrite arm spacings with decreasing specimen wall thickness. This was explained by an increasing heat transfer by thermal radiation with decreasing wall thicknesses of the specimens.<sup>[10]</sup>

Possible physical origins of this anisotropic effect during directional solidification in the Bridgman process are as follows. Goldschmidt<sup>[20]</sup> as well as Zhang et al.<sup>[10]</sup> argued that a decreasing primary dendrite spacing could simply relate to locally increased temperature gradients in thin-walled specimens with decreasing wall thickness. Konrad et al.<sup>[12]</sup> determined a temperature drop of 89 °C at the interface between the ceramic mold and the melt. The heat dissipation at the interface between the ceramic mold and the melt is higher, which may lead to local higher lateral temperature gradients in  $x$ - and  $y$ -directions at positions next to the ceramic mold/cast interfaces. This results in an  $\approx 0.2$  mm thin anisotropic boundary zone, which could explain the observed decrease in the primary dendrite arm spacing. This boundary zone also exists in the single-crystal cylindrical specimens with a diameter of 15 mm. This is schematically illustrated for the casting geometry with a thin-walled section of 0.4 and 2 mm by **Figure 8**. The anisotropic arrangement of the primary dendrites, which is characterized by smaller primary dendrite arm spacings in the boundary zone, is illustrated by a schematic illustration in **Figure 8b**.

From the studies presented in **Figure 6** and **7**, we conclude that within the boundary zone next to the ceramic mold, the average primary dendrite arm spacing is anisotropic. The anisotropic reduction of the primary dendrite arm spacing leads to significantly lower average values within these boundary zones, located next to the ceramic mold, see **Figure 7**. This  $\approx 0.2$  mm thin boundary zone of anisotropic primary dendrite arm spacings is not only evident in the thin-walled single-crystal specimens, but also in the cylindrical specimen. However, the thinner the casting geometry, the larger the fraction of the boundary zone with respect to the total volume of the cast specimens and the more important is this anisotropic reduction of the primary dendrite arm spacing for the overall properties.

As a general introduction to this ongoing topic of intense research, we refer to the recent review papers on directional dendritic solidification and primary dendrite arm spacings.<sup>[3,21–23]</sup> During solidification, two neighboring dendrites also compete with each other for solute atoms out of the melt. This competition results in a complex interaction between the two dendritic trunks, which is mediated by the surrounding liquid concentration field. The primary dendrite arm spacing is a result of this complex interaction. Of course, also the present observation of reduced anisotropic primary dendrite arm spacings in the boundary zone relates to this complex interaction, as the solute competition is fundamentally different at the mold/cast interface as compared with the inner of the cast. Remarkable progress was made in the field of dendritic solidification in recent years using sophisticated models and detailed computer simulations, such as phase-field models or more coarse-grained approaches.<sup>[23]</sup> Finite-element simulations of the single-crystal solidification represent a possible solution for further investigation of the anisotropic growth of the primary dendrite arms. This allows predictions regarding the established temperature profiles depending on the specimen geometry and the resulting microstructure.

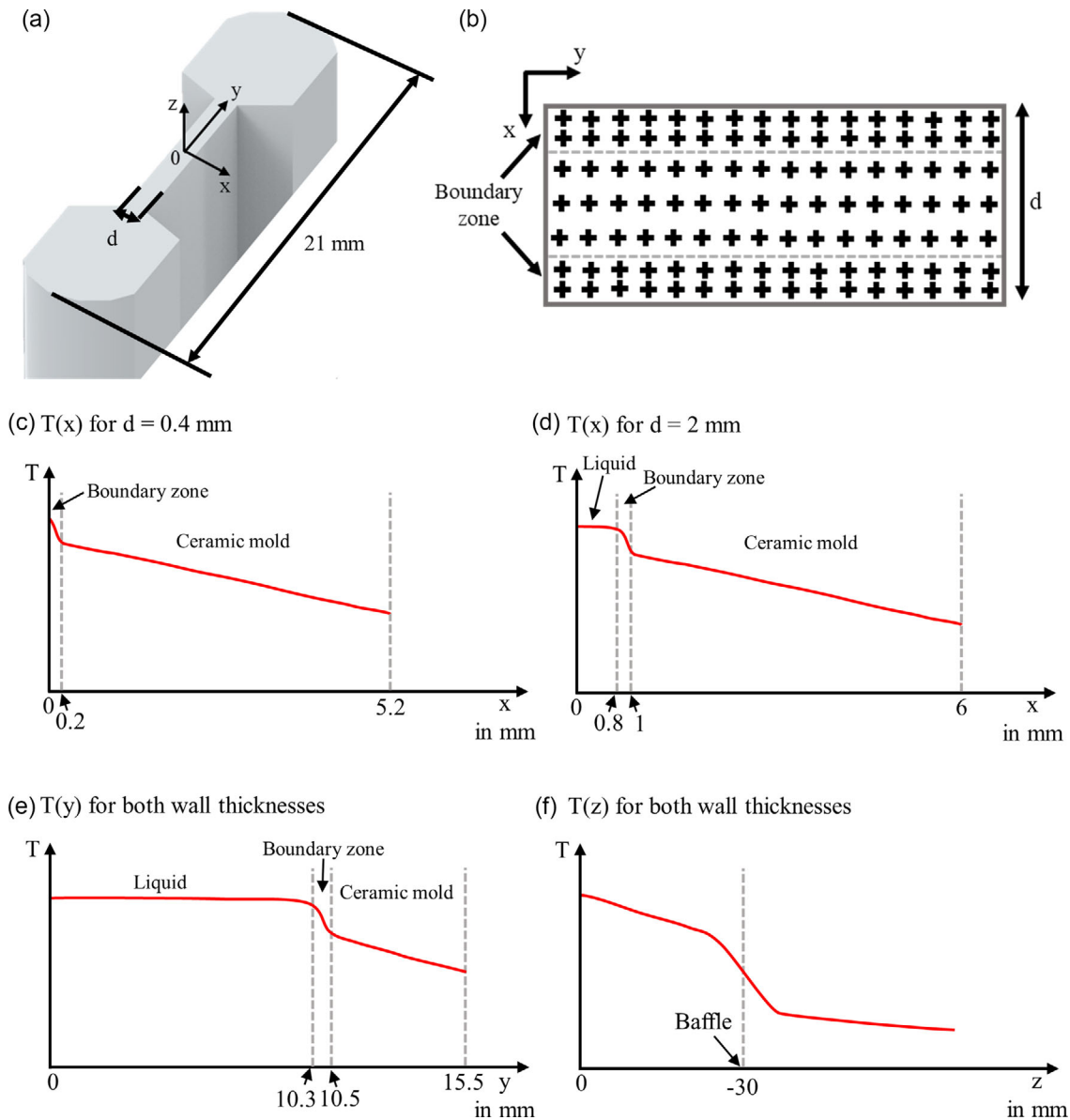


**Figure 8.** a) Sketch of the casting geometry of a thin-walled specimen including a coordinate system in the middle of the specimen to define the three directions. b) Schematic illustration of the anisotropic arrangement of the primary dendrites in the boundary zone. Schematic illustration of the temperature distribution as a function of the distance to the center of the thin-walled specimen in c)  $x$ -direction for  $d = 0.4$  mm, d)  $x$ -direction for  $d = 2$  mm, e)  $y$ -direction for both wall thicknesses, and f)  $z$ -direction for both wall thicknesses. c–e) An increased temperature gradient in the boundary zone due to higher heat dissipation by the ceramic mold.

## 5. Conclusion

Primary and secondary dendrite arm spacings were determined as a function of the withdrawal rate and the cast wall thickness. In addition to conventional single-crystal cylindrical specimens with 15 mm diameter, thin-walled single-crystal specimens with different wall thicknesses of 0.4, 0.8, 1, and 2 mm were cast from the nickel-based superalloy MAR M247LC. 1) The usually expected withdrawal rate dependence during single-crystal casting also applies to thin-walled specimens: increasing withdrawal

rates lead to decreasing primary ( $\lambda_p \sim v^{-1/4}$ ) and secondary ( $\lambda_s \sim v^{-1/3}$ ) dendrite arm spacings. 2) The primary dendrite arm spacing decreases slightly with decreasing wall thickness, whereas the secondary dendrite arm spacing is relatively independent of the wall thickness. 3) An anisotropy of the primary dendrite arm spacing is observed due to smaller spacings in  $x$ -direction. 4) Anisotropic primary dendrite arm spacings are particularly in the boundary zones, which extend up to 0.2 mm in size inward from the surface. This boundary zone is also present within the cylindrical specimens with 15 mm diameter.

## Acknowledgements

The German research foundation (DFG) is gratefully acknowledged for funding the research project GL181/52-1.

Open access funding enabled and organized by Projekt DEAL.

## Conflict of Interest

The authors declare no conflict of interest.

## Data Availability Statement

The data that support the findings of this study are available from the corresponding author upon reasonable request.

## Keywords

dendrite arm spacings, directional solidification, Ni-based superalloys, single crystals, thin walled

Received: September 29, 2021

Revised: December 16, 2021

Published online:

- [1] K. F. O'Connor, J. P. Hoff, D. J. Frasier, R. E. Peeler, H. Mueller-Largent, F. F. Trees, J. R. Whetstone, J. H. Lane, E. Jeffries, *US 6255000 B1, Allison Engine Company, Inc.*, **2001**.
- [2] H. Klingels, A. Platz, *DE 102006050440 A1, MTU Aero Engines GmbH*, **2013**.
- [3] J. Strickland, B. Nenchev, H. Dong, *Crystals* **2020**, *10*, 1.
- [4] M. M. Franke, M. Hilbinger, A. Heckl, R. F. Singer, *Adv. Mater. Res.* **2011**, *278*, 156.
- [5] M. M. Franke, R. M. Hilbinger, C. H. Konrad, U. Glatzel, R. F. Singer, *Metall. Mater. Trans. A* **2011**, *42*, 1847.
- [6] M. Grudzień-Rakoczy, Ł. Rakoczy, R. Cygan, F. Kromka, Z. Pirowski, O. Milkovič, *Materials* **2020**, *13*, 1.
- [7] G. Liu, L. Liu, C. Ai, B. Ge, J. Zhang, H. Fu, *Alloys Compd.* **2011**, *509*, 5866.
- [8] S. Milenkovic, I. Sabirov, J. Llorca, *Mater. Lett.* **2012**, *73*, 216.
- [9] J. S. Lee, J. H. Gu, H. M. Jung, E. H. Kim, Y. G. Jung, J. H. Lee, *Mater. Today Proc.* **2014**, *1*, 3–10.
- [10] P. Zhang, X. Gong, B. Li, X. Song, G. Yang, F. Tao, *Energy Mater. Conf. Proc.* **2014**, 381.
- [11] J. Krawczyk, W. Bogdanowicz, *Materials* **2021**, *14*, 1.
- [12] C. H. Konrad, M. Brunner, K. Kyrgyzbaev, R. Völkl, U. Glatzel, *J. Mater. Process. Technol.* **2011**, *211*, 181.
- [13] S. Körber, R. Völkl, U. Glatzel, *J. Mater. Process. Technol.* **2021**, *293*, 117095.
- [14] H. Jacobi, K. Schwerdtfeger, *Metall. Trans. A.* **1976**, *7*, 811.
- [15] P. R. Sahm, I. Egly, T. Volkmann, in *Schmelze, Erstarrung, Grenzflächen*, Springer, Berlin Heidelberg **1999**.
- [16] A. J. Elliott, S. Tin, W. T. King, S. C. Huang, M. F. X. Gigliotti, T. M. Pollock, *Metall. Mater. Trans. A* **2004**, *35*, 3221.
- [17] Y. Zhou, A. Volek, R. F. Singer, *Metall. Mater. Trans. A* **2005**, *36A*, 651.
- [18] H. S. Whitesell, L. Li, R. A. Overfelt, *Metall. Mater. Trans. B* **2000**, *31*, 546.
- [19] H. S. Whitesell, R. A. Overfelt, *Mater. Sci. Eng. A* **2001**, *318*, 264.
- [20] D. Goldschmidt, *Mater. Sci. Eng. Tech.* **1994**, *25*, 311.
- [21] D. Tourret, A. Karma, *Acta Mater.* **2016**, *120*, 240.
- [22] W. Kurz, D. J. Fisher, in *Fundamentals of Solidification*, Trans Tech Publications Ltd, Uetikon-Zuerich **1998**.
- [23] W. Kurz, D. J. Fisher, R. Trivedi, *Int. Mater. Rev.* **2019**, *64*, 311.